Unsteady Transonic Flow Calculations for Wing/Fuselage Configurations

John T. Batina*
NASA Langley Research Center, Hampton, Virginia

Unsteady transonic flow calculations are presented for wing/fuselage configurations. Calculations are performed by extending the XTRAN3S (version 1.5) unsteady transonic small-disturbance code to allow the treatment of a fuselage. The research was conducted as part of a larger effort directed toward developing the capability to treat a complete flight vehicle. Details of the XTRAN3S fuselage modeling are discussed in the context of the small-disturbance equation. Transonic calculations are presented for two wing/fuselage configurations with leading-edge sweep angles of 0 and 36.65 deg, the results of which compare well with available experimental steady-pressure data. Unsteady calculations are performed for simple bending and torsion modal oscillations of the wing. Comparisons of sectional lift and moment coefficients for the wing-alone and wing/fuselage cases reveal effects of fuselage aerodynamic interference on the unsteady wing loading. Tabulated generalized aerodynamic forces, typically used in flutter analyses, indicate small changes in the real (in-phase) component and as much as a 30% change in the imaginary (out-of-phase) component when the fuselage is included in the calculation. These changes result in a 2–5% increase in total magnitude and a several degree increase in phase.

Nomenclature

A_{ij} = generalized aerodynamic force resulting from pressure induced by mode j acting through displacements of mode i
$\mathcal{R}$ = full-span aspect ratio
c = airfoil chord
c_ℓ = sectional lift coefficient
c_m = sectional pitching moment coefficient about local midchord
c_r = reference chord
C_p = pressure coefficient
F = fuselage fineness ratio
k = reduced frequency, $\omega c_r/2U$
L = fuselage length
M = freestream Mach number
TR = taper ratio
t = time, nondimensionalized by freestream velocity and reference chord
U = freestream velocity
α_F = fuselage angle of attack
α_W = wing angle of attack
γ = ratio of specific heats
Δt = nondimensional time step
Λ = sweep angle of wing leading edge
$\bar{\eta}$ = fractional semispan
ϕ = disturbance velocity potential
ω = angular frequency

Received April 24, 1986; presented as Paper 86-0862 at the AIAA/ASME/ASCE/AHS 27th Structures, Structural Dynamics and Materials Conference, San Antonio, TX, May 19-21, 1986; revision received Aug. 12, 1986.

*Research Scientist, Unsteady Aerodynamics Branch, Loads and Aeroelasticity Division. Senior Member AIAA.

Introduction

COMPUTATIONAL methods for predicting flowfields about wing/fuselage and multiple component configurations have been developed over recent years (see Refs. 1-9, for example). Techniques based on the doublet lattice method and the method of images have been reported by Giesing et al.[1] for calculating steady and oscillatory aerodynamics for interfering wings and bodies. Computer programs based on panel methods such as that developed by Woodward[2,3] may be used for analyzing wing/body/tail configurations. More recently, computer programs such as PANAIR[4] have been developed for the analysis of complete flight vehicles. However, the underlying linear theory on which these methods are based restricts the applications to subsonic and supersonic flows.

At transonic speeds, finite-difference methods are generally employed for the computation of transonic flows about wing/fuselage configurations. In the context of the transonic small-disturbance (TSD) equation, for example, Bailey and Ballhaus[5] calculated the transonic flow about nonlifting wing/cylinder combinations using a relaxation method. Steady pressure distributions were presented for a 30-deg swept wing on straight and area-ruled cylinders. Klunker and Newman[6] reported steady pressure results for a lifting wing centrally mounted on a cylindrical body. A coordinate transformation simplified the fuselage flow-tangency boundary condition and line relaxation was used to solve the TSD equation. Bailey and Ballhaus[7] continued their work of Ref. 5 to treat nonlifting wings mounted on finite-length fuselages. The computed results compared well with experimental data for both rectangular and swept wing/fuselage configurations at transonic Mach numbers. Boppe[8] extended these relaxation methods to compute transonic flows about realistic wing/fuselage configurations using a grid embedding technique. The method can treat configurations with arbitrary fuselage shapes since details of the flow are resolved using a locally embedded fine grid. In Ref. 8, steady transonic calculations for several wing/fuselage configurations showed excellent agreement with experimental data. Boppe and Stern[9] have extended the method of Ref. 8 to treat fairly complex aircraft configurations by including nacelles, pylons, and winglets in the analysis.

Although the finite-difference methods based on the TSD equation are applicable to transonic wing/fuselage cases, the

solution techniques are restricted to steady flows. Solutions for unsteady transonic flowfields have recently been made possible using computer codes such as XTRAN3S.[10] The XTRAN3S unsteady TSD code was developed by the Boeing Military Airplane Company under U.S. Air Force contract and is the most fully developed U.S. code for transonic aeroelastic analysis of isolated planar wings. Because of the need to be able to perform aeroelastic analyses for complete aircraft configurations, XTRAN3S is being modified to enable treatment of additional aircraft components such as the fuselage, canard, tail, pylons, nacelles, stores, and control surfaces. The capability to treat multiple lifting surface configurations such as closely coupled canard/wing and wing/tail geometries has already been developed and reported by the author.[11]

The purpose of the present paper is to present the development of the XTRAN3S wing/fuselage capability for predicting transonic unsteady aerodynamic loads for aeroelastic applications. The objectives of the research were to: 1) modify the XTRAN3S code to allow the treatment of a fuselage, 2) validate the method by making comparisons with available experimental data, and 3) investigate and demonstrate the effects of fuselage aerodynamic interference on transonic pressures and forces on the wing. The paper presents a description of the XTRAN3S wing/fuselage modeling along with the results and comparisons assessing the new capability.

Computational Procedures

In this section, version 1.5 of the XTRAN3S transonic code[12] is briefly described. A discussion of fuselage modeling and the development of the XTRAN3S wing/fuselage capability are also given.

XTRAN3S Transonic Code

The XTRAN3S code provides a time-accurate, finite-difference solution to the nonlinear, small-disturbance potential equation for transonic flow. The code can be used to calculate steady and unsteady transonic flowfields about planar wings including aeroelastic deformation effects. The program is capable of treating either forced harmonic or aeroelastic transient type motions. A time-accurate alternating-direction implicit (ADI) finite-difference algorithm is used to solve the modified transonic small-disturbance equation

$$M^2(\phi_t + 2\phi_x)_t = [(1-M^2)\phi_x - \tfrac{1}{2}(\gamma+1)M^2\phi_x^2 + \tfrac{1}{2}(\gamma-3)M^2\phi_y^2]_x + [\phi_y - (\gamma-1)M^2\phi_x\phi_y]_y + (\phi_z)_z \quad (1)$$

where x, y, and z are the nondimensional physical coordinates in the streamwise, spanwise, and vertical directions, respectively. Details of the solution procedure and the boundary conditions imposed upon the flowfield are given in Ref. 10. The coordinate transformation used to treat swept tapered lifting surfaces may be found in Ref. 12.

Fuselage Modeling

In this study, the ADI solution procedure of the XTRAN3S code has been extended to allow the treatment of a fuselage. A discussion of fuselage modeling in small-disturbance codes and the development of the XTRAN3S wing/fuselage capability follow.

For a fuselage at angle of attack α_F with unit normal vector $n = (n_x, n_y, n_z)$, the small-disturbance fuselage flow-tangency boundary condition may be written as

$$\phi_n = n_x + n_y\phi_y + n_z(\phi_z + \alpha_F) = 0 \quad (2)$$

where ϕ_n is the velocity normal to the surface. This boundary condition may be implemented in several different ways. For example, Eq. (2) may be imposed at boundary grid points identified to be in close proximity to the fuselage surface as done by Bailey and Ballhaus.[7] This method requires that a grid be constructed such that points lie very close to the fuselage surface. This requirement is restrictive, however, since it is difficult to construct such a grid in a Cartesian domain. Boppe[8] addressed the problem by imposing the fuselage boundary condition on a constant cross-sectional computational surface rather than on the true fuselage surface. The computational surface extends from upstream infinity to downstream infinity, the cross section of which approximates the fuselage shape at the maximum fuselage diameter. The technique is consistent with the small-disturbance approximation and, since there is no requirement to locate grid points close to the fuselage surface, the method provides a "hands-off" representation for modeling wing/fuselage configurations.

A further simplification to the implementation of Eq. (2) has been reported by Mason et al.[13] in the user's manual for the Bailey/Ballhaus code. In Ref. 13, a fixed rectangular cross section is used for the computational fuselage surface as shown in Fig. 1, rather than a shape determined at the maximum fuselage diameter. The advantage of this treatment is the simplification to the fuselage boundary condition [Eq. (2)] that results. Along the side boundary of the rectangular computational surface, Eq. (2) is approximated by

$$\phi_y = \frac{\Delta C}{\Delta \bar{C}} F_y \quad (3a)$$

and along the top and bottom surfaces, Eq. (2) is approximated by

$$\phi_z = \frac{\Delta C}{\Delta \bar{C}} F_z - \frac{S}{\bar{S}}\alpha_F \quad (3b)$$

where $F_y = -n_x/n_y$ and $F_z = -n_x/n_z$. These simplified fuselage boundary conditions are analogous to the wing flow-tangency boundary condition that is imposed on the mean plane of the wing rather than on the true wing surface. To account for spatial differences between true and computational fuselage surfaces, slender-body theory corrections modify the fuselage thickness and angle-of-attack terms that appear on the right-hand sides of Eqs. (3). In Eqs. (3), ΔC and $\Delta \bar{C}$ are arclengths of the true and computational fuselage surfaces, respectively, as graphically defined in Fig. 1, S and $\bar{S}$ are the cross-sectional areas of the true and computational surfaces, respectively.

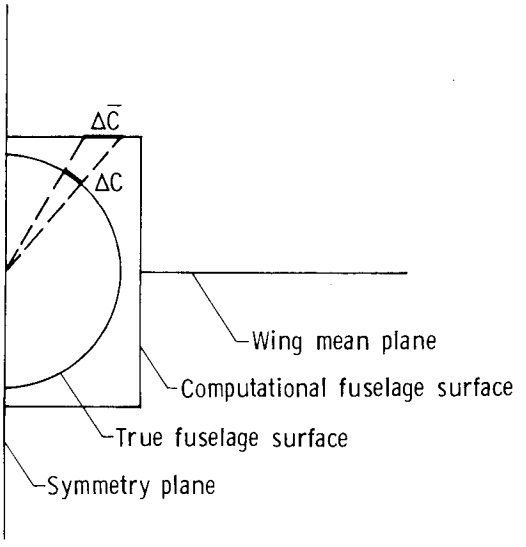

Fig. 1 Definition of arclengths on true and computational fuselage surfaces.

Following Ref. 13, the boundary conditions [Eqs. (3)] have been incorporated in an implicit finite-difference fashion. This treatment of the fuselage imposes the boundary conditions directly within the ADI algorithm, which is in contrast with an approximate treatment using extrapolated differencing. Details of the numerical implementation of the fuselage boundary conditions and the finite-difference grids are contained in Ref. 17.

Structural Modes

Unsteady transonic calculations were performed for first bending and first torsion modal oscillations of the wing. For demonstration purposes, simple polynomial equations were assumed to describe the modes. The equation defining the first bending mode shape was derived by assuming that the node line is perpendicular to the wing midchord line at the root. The resulting expression for the first bending mode shape is given by

$$f_h = (y-y_r)\,[(X-\tfrac{1}{2})\,\sin\Lambda_{c/2} + (y-y_r)\,\cos\Lambda_{c/2}] \quad \text{for } y \geq y_r \tag{4}$$

where y_r is the spanwise coordinate of the wing root and $\Lambda_{c/2}$ is the sweep angle of the wing midchord line. The equation defining the first torsion mode shape, derived by assuming that the node line coincides with the wing midchord line, is given by

$$f_\alpha = (y-y_r)\,[(X-\tfrac{1}{2})\,\cos\Lambda_{c/2} - (y-y_r)\,\sin\Lambda_{c/2}] \quad \text{for } y \geq y_r \tag{5}$$

Equations (4) and (5) were normalized to give unit deflection and unit twist, respectively, at the tip. The tip amplitude of the torsion mode was selected as 1 deg and the amplitude of the bending mode was calculated to be an equivalent effective angle of attack using $\dot{h}_{tip}/U = 1$ deg.

Results and Discussion

Configurations

Results are presented for the two wing/fuselage configurations shown in Fig. 2. These configurations were selected to assess the fuselage treatment and verify the code modifications to XTRAN3S by making comparisons with the experimental steady pressure data of Refs. 14 and 15. The first configuration (Fig. 2a) is the wall interference model[14] tested at the Arnold Engineering Development Center (AEDC) (hereafter referred to as the AEDC wing/fuselage), which consists of a rectangular-planform wing that is centrally mounted on a circular cross-sectional sting body. As listed in Fig. 2a, the wing has an NACA 63A006 airfoil section, a leading-edge sweep angle of 0 deg, a full-span aspect ratio of 3.56, and a taper ratio of 1.0. The axisymmetric fuselage has a fineness ratio (length/maximum diameter) of 8.42. A more detailed description of the AEDC wing/fuselage is reported in Ref. 14 along with the experimental data. The second configuration, shown in Fig. 2b, is a transport-type wing/fuselage model that was tested in the Royal Aircraft Establishment (RAE) 8 ft×6 ft transonic wind tunnel. This model (hereafter referred to as the RAE wing/fuselage) is a standard configuration of the AGARD Fluid Dynamics Panel and consists of the RAE wing "A" in combination with an axisymmetric body.[15] As listed in Fig. 2b, the wing of the RAE wing/fuselage has an RAE 101 airfoil section, a leading-edge sweep angle of 36.65 deg, an aspect ratio of 6.0, and a taper ratio of one-third. The fuselage has a fineness ratio of 7.66 and a constant diameter from 0.35–1.0 L. The fuselage is mounted to the sting using a short tapered section as shown in Fig. 2b. Although the stings for the two wing/fuselage configurations are modeled using XTRAN3S, the short tapered section connecting the fuselage of the RAE model to the sting was not. This section was neglected to minimize the cost of the calculations since fewer gridpoints are required. Furthermore, no experimental data were measured aft of 0.83L on the fuselage.

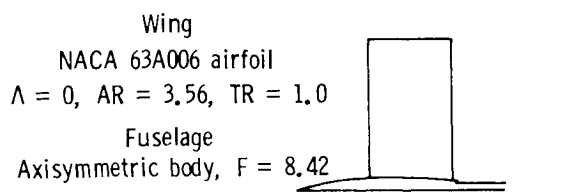

a) AEDC.

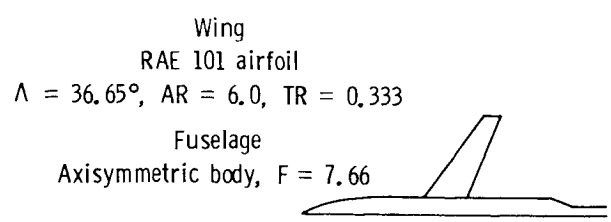

b) RAE.

Fig. 2 Wing/fuselage configurations.

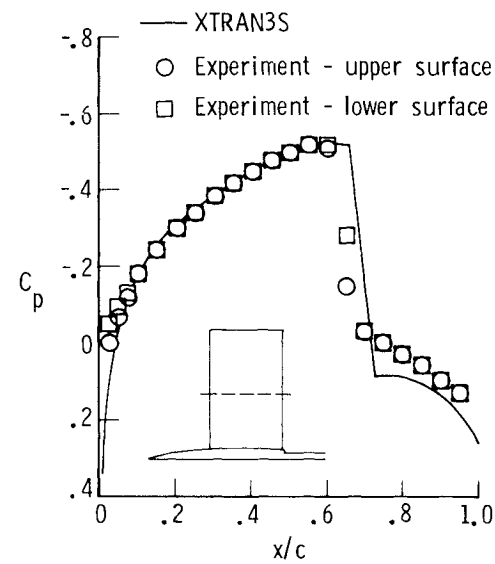

a) Wing midsemispan.

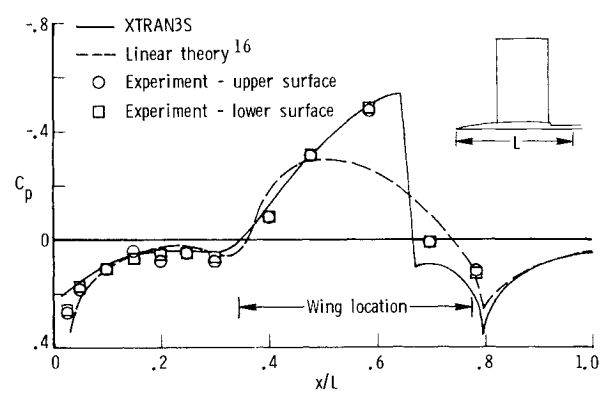

b) Fuselage symmetry plane.

Fig. 3 Comparison between XTRAN3S and experimental steady pressure distributions on the AEDC wing/fuselage at $M = 0.9$ and $\alpha_W = \alpha_F = 0$.

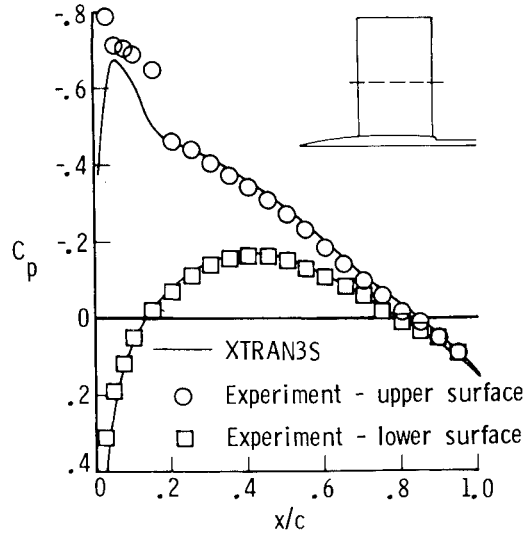

a) Wing midsemispan.

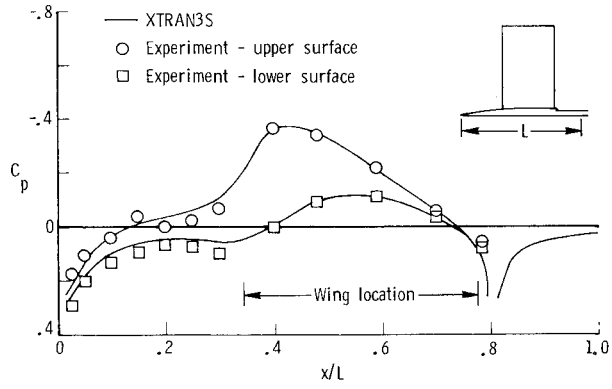

b) Fuselage symmetry plane.

Fig. 4 Comparison between XTRAN3S and experimental steady pressure distributions on AEDC wing/fuselage at $M=0.8$ and $\alpha_W=\alpha_F=2.663$ deg.

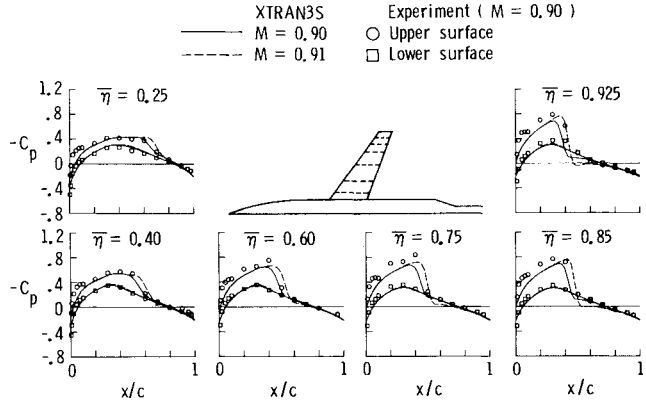

Fig. 5 Comparison between XTRAN3S and experimental wing steady pressure distributions on RAE wing/fuselage at $M=0.90$ and 0.91 and $\alpha_W=\alpha_F=1$ deg.

Table 1 Wing/fuselage configurations and computational conditions for transonic aerodynamics analyses

Wing/fuselage	Case	M	α_W, α_F, deg
AEDC	1	0.9	0
	2	0.8	2.663
RAE	3	0.90, 0.91	1

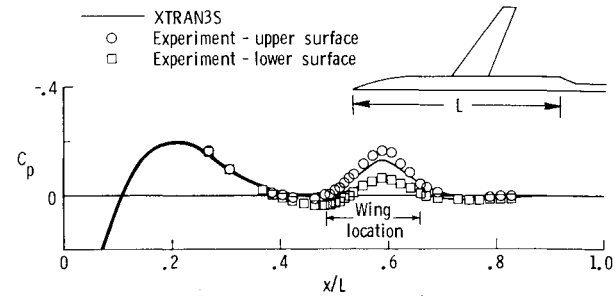

Fig. 6 Comparison between XTRAN3S and experimental fuselage symmetry plane steady pressure distributions on RAE wing/fuselage at $M=0.9$ and $\alpha_W=\alpha_F=1$ deg.

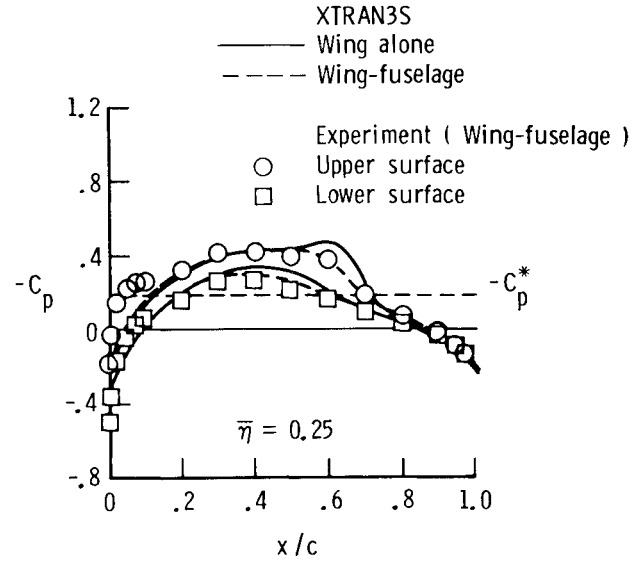

Fig. 7 Wing steady pressure distributions for RAE wing/fuselage at $M=0.9$, $\alpha_W=\alpha_F=1$ deg, and $\bar{\eta}=0.25$.

AEDC Wing/Fuselage

Steady transonic calculations were performed for the AEDC wing/fuselage for comparison with the experimental data of Ref. 14. The experimental steady pressure data was measured at the midsemispan of the wing and the fuselage symmetry plane only. Two cases were considered to validate the XTRAN3S wing/fuselage capability. The first case, Case 1 of Table 1, was chosen to assess the XTRAN3S fuselage thickness modeling by selecting zero mean angle of attack for the wing and fuselage. Case 2 was selected to assess the fuselage angle-of-attack modeling. For both cases, the time step was $\Delta t=0.05$ and 800 steps were required for the solution to converge.

In Case 1, the freestream Mach number was 0.9 and $\alpha_W=\alpha_F=0$. Comparisons between XTRAN3S and experimental steady pressure distributions are shown in Figs. 3a and 3b for the wing and fuselage, respectively. For the wing (Fig. 3a), the XTRAN3S pressures compare well with the experimental data. There is a relatively strong shock wave on the upper and lower surfaces near 65-70% chord. The XTRAN3S comparison with experiment is typical for a conservative inviscid TSD code in that the calculated shocks are located slightly aft of the experimental location and the postshock pressures are slightly overpredicted. For the fuselage (Fig. 3b), the symmetry plane pressure distribution resembles that of the wing in the region of the wing location and there is a relatively strong shock wave on the fuselage upper and lower surfaces near 0.66L. The XTRAN3S

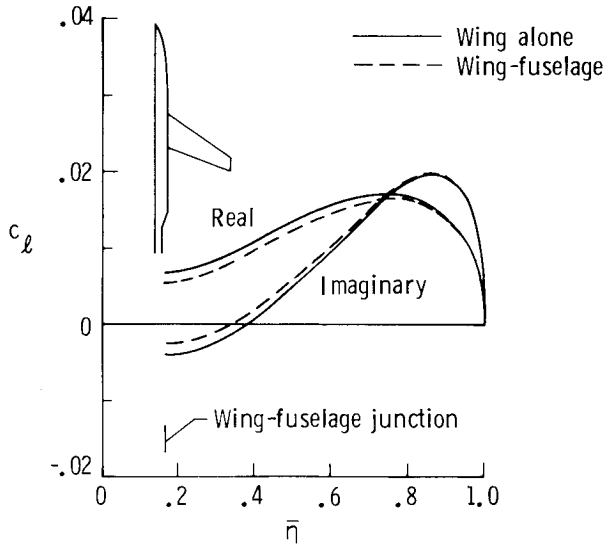

a) Sectional lift coefficients.

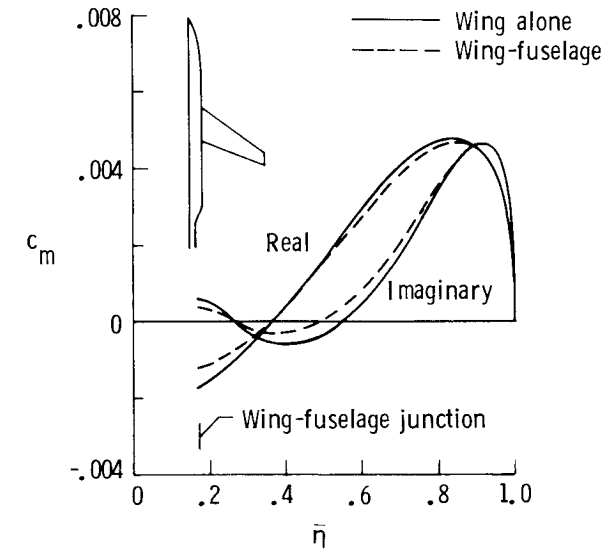

b) Sectional moment coefficients.

Fig. 8 Unsteady sectional coefficients due to wing first bending for the RAE wing/fuselage at $M=0.91$, $\alpha_W=\alpha_F=1$ deg, and $k=0.25$.

fuselage pressure distribution is in good agreement with the experimental data. This agreement is as good as that for the wing, thus verifying the fuselage thickness modeling. Also, linear theory results from Ref. 16, computed using the Woodward[3] panel code, are presented in Fig. 3b for further comparison. The linear theory results compare well with the experimental pressures, except in the wing location region where transonic effects are important.

In Case 2, the freestream Mach number was 0.8 and the experimental data were obtained at 2 deg angle of attack. However, the calculations were performed at a corrected angle of attack of 2.663 deg to include the static deformation of the sting under load.[16] The wing midsemispan and fuselage symmetry plane steady pressure distributions are shown in Figs. 4a and 4b, respectively. For the wing (Fig. 4a), the XTRAN3S pressures are in good general agreement with the experimental data except for a slight underprediction of the leading-edge suction peak on the upper surface. For the fuselage (Fig. 4b), the XTRAN3S calculations compare very well with the experimental steady pressure data along both the upper and lower fuselage surfaces. The good agreement between XTRAN3S and experimental symmetry plane pressures thus verifies the fuselage angle-of-attack modeling.

RAE Wing/Fuselage

Transonic calculations were performed for the RAE wing/fuselage to assess further the wing/fuselage capability by making comparisons with the experimental steady pressure data of Ref. 15. The case selected, Case 3 of Table 1, corresponds to the wing/fuselage at 1 deg angle of attack. The time step was $\Delta t=0.025$ and 1600 steps were used to obtain a converged solution. The experimental data was measured at a freestream Mach number of 0.9 and the calculations were performed at both $M=0.9$ and 0.91. Calculations were made at the latter Mach number, since it was shown in Ref. 13 that results computed using the Bailey/Ballhaus code for the RAE wing/fuselage at $M=0.91$ were in better agreement with the experimental data than results computed at $M=0.9$.

Steady pressure distributions for six span stations along the wing of the RAE wing/fuselage are shown in Fig. 5 for Case 3. There is a shock wave on the upper surface of the wing that is relatively mild in the inboard region and is of moderate strength outboard toward the wing tip. In general, the XTRAN3S steady pressures are in good agreement with the experimental data. The calculations at $M=0.9$ compare better with the experiment in the inboard region of the wing (at $\bar{\eta}=0.25$, for example), but the calculated results at $M=0.91$ are generally what is expected from a conservative inviscid TSD code in comparison with the experiment. For example, the shock wave on the wing upper surface calculated at $M=0.91$ is located slightly aft of the experimental location and the postshock pressures are overpredicted. For cases such as this, the inclusion of the nonisentropic effects and viscous effects are required to improve the correlation between calculation and experiment. Figure 6 shows the fuselage symmetry plane steady pressure distributions at $M=0.9$ and $\alpha_W=\alpha_F=1$ deg. There is a large pressure expansion from 0.11-0.40L due to the sloped nose of the fuselage. Also, the fuselage carries a small amount of lift in the wing location region. In general, the XTRAN3S fuselage pressures are in good agreement with the experimental data. Steady pressure distributions at $\bar{\eta}=0.25$ of the wing are presented in Fig. 7 for Case 3. The calculated pressure distributions for $M=0.9$ are plotted for the wing-alone and wing/fuselage configurations for comparison with the experimental data. As shown in Fig. 7, the fuselage interference weakens the mild shock wave on the wing upper surface, bringing the XTRAN3S steady pressures into very good agreement with the experiment.

Unsteady transonic calculations were performed for the RAE wing/fuselage to demonstrate application of the new capability to aeroelastic problems. Experimental data for this model are not available for comparison purposes. The freestream Mach number was selected as $M=0.91$ and $\alpha_W=\alpha_F=1$ deg (Case 3). The wing was first forced to oscillate harmonically in first bending and then in first torsion at a reduced frequency of $k=0.25$. The time step was $\Delta t=0.02513$, which results in 500 steps per cycle of motion. Three cycles of motion were computed to obtain a periodic solution.

Unsteady sectional lift and moment coefficients are shown in Figs. 8a and 8b, respectively, for the wing oscillating in its first bending mode. These coefficients are plotted as real (in-phase) and imaginary (out-of-phase) components of the spanwise wing loading. The unsteady coefficients are largest in the outboard region of the wing since the wing motion is largest at the tip. The effect of fuselage aerodynamic interference is generally largest inboard toward the wing/fuselage junction, as expected. As shown in Fig. 8a, for example, the fuselage interference decreased the mag-

Table 2 Generalized aerodynamic forces for RAE wing/fuselage at $M=0.91$, $\alpha_W=\alpha_F=1$ deg, and $k=0.25$ (mode 1: bending, mode 2: torsion)

A_{ij}		Wing alone				Wing/fuselage							
i	j	Real	Imag	Mag	Phase, deg	Real	Increase, %	Imag	Increase, %	Mag	Increase, %	Phase, deg	Increase, deg
1	1	0.230	0.254	0.343	47.8	0.227	−1.3	0.270	6.3	0.353	2.9	49.9	2.1
1	2	0.841	−0.101	0.847	−6.9	0.858	2.0	−0.071	−29.7	0.861	2.4	−4.7	2.2
2	1	0.037	0.011	0.039	17.0	0.038	2.7	0.014	27.3	0.041	5.1	19.9	2.9
2	2	0.095	−0.076	0.121	−38.6	0.101	6.3	−0.073	−3.9	0.124	2.5	−35.7	2.9

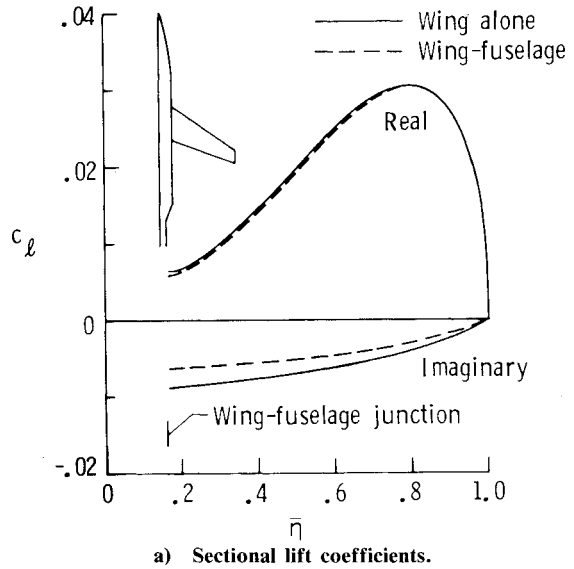

a) Sectional lift coefficients.

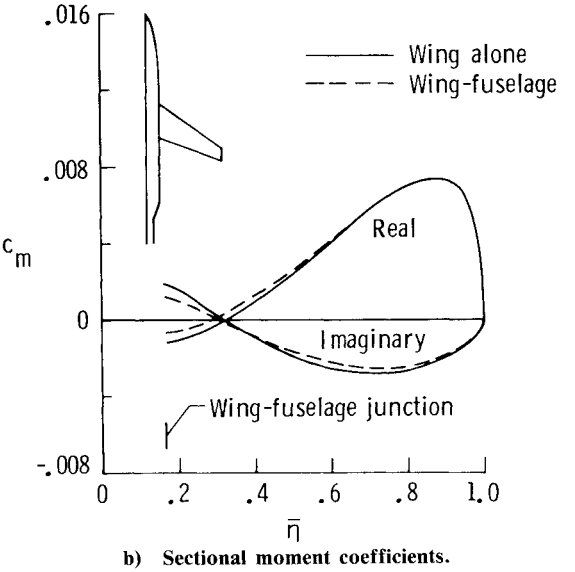

b) Sectional moment coefficients.

Fig. 9 Unsteady sectional coefficients due to wing first torsion for the RAE wing/fuselage at $M=0.91$, $\alpha_W=\alpha_F=1$ deg, and $k=0.25$.

nitudes of the real and imaginary lift coefficients by 19 and 37%, respectively, near the wing/fuselage junction. The interference effect attenuates along the span and is negligible outboard toward the wing tip. The effect of the fuselage on the unsteady sectional moment coefficients (Fig. 8b) is similar to that on the lift coefficients. The magnitudes of the real and imaginary components of c_m are decreased near the wing/fuselage junction for the wing/fuselage configuration and the effect generally decreases spanwise, vanishing near the tip.

Unsteady sectional lift and moment coefficients are shown in Figs. 9a and 9b, respectively, for the wing oscillating in its first torsion mode. These coefficients are similar in character to the coefficients of Fig. 8 in that the largest magnitudes generally occur in the outboard region and the effects of fuselage aerodynamic interference are greatest in the inboard region near the wing/fuselage junction. As shown in Fig. 9a, for example, the fuselage interference slightly lowers the real part of c_ℓ and significantly decreases the magnitude of the imaginary part. This result is attributed physically to the weakening of the steady shock on the wing by the presence of the fuselage as shown in the steady pressure distributions of Fig. 7. For the moment coefficients (Fig. 9b), the fuselage interference decreased the magnitudes of the real and imaginary components near the wing/fuselage junction. Outboard on the wing, the effect of the fuselage is small.

Generalized aerodynamic forces were then calculated by integrating the unsteady lifting pressures, weighted by the mode shapes, over the wing planform. These forces A_{ij} are typically used in flutter analyses and are defined as the forces resulting from the pressure induced by mode j acting through the displacements of mode i. In this study, bending and torsion are defined as modes 1 and 2, respectively. The generalized aerodynamic forces are listed in Table 2 for both the wing-alone and wing/fuselage cases. Results are tabulated in both real/imaginary and magnitude/phase forms to allow for a fair and complete assessment of fuselage aerodynamic interference. Comparisons between the forces indicate relatively small changes in the real components and generally much larger changes in the imaginary components when the fuselage is included in the calculation. For example, the imaginary part of A_{12} is decreased 29.7% and the imaginary part of A_{21} is increased 27.3%. In general, though, the changes in the generalized aerodynamic forces occur such that the total magnitude is increased 2–5%, and the phase is increased 2–3 deg.

Conclusions

A time-accurate transonic wing/fuselage capability has been developed for unsteady aerodynamic and aeroelastic applications. The new capability was developed by extending the XTRAN3S unsteady transonic small-disturbance code to allow the treatment of a fuselage. The code is now capable of computing unsteady transonic flowfields about wing/fuselage configurations. The capability permits the assessment of fuselage aerodynamic interference effects on transonic unsteady airloads and flutter characteristics of wings.

Steady transonic calculations were presented for two wing/fuselage geometries with leading-edge sweep angles of 0 and 36.65 deg and comparisons were made with experimental pressure data for code validation purposes. The XTRAN3S wing and fuselage pressure distributions were in good agreement with the experimental data. These favorable comparisons thus verify the fuselage treatment and code modifications to XTRAN3S and also demonstrate the accuracy of the code for wing/fuselage applications.

Unsteady transonic calculations were presented for a transport-type wing/fuselage configuration. The calculations

were performed for simple first bending and first torsion structural modes that were assumed for the wing. Comparisons of unsteady sectional lift and moment coefficients for the wing-alone and wing/fuselage cases revealed effects of fuselage aerodynamic interference on the unsteady wing loading. In general, the interference of the fuselage decreased the magnitudes of the lift and moment coefficients near the wing/fuselage junction. The effect of the fuselage on the unsteady wing loading decreased outboard toward the wing tip, as expected. Tabulated generalized aerodynamic forces, typically used in flutter analyses, indicated small changes in the real component and as much as a 30% change in the imaginary component when the fuselage was included in the calculation. These changes resulted in a 2-5% increase in total magnitude and a several degree increase in phase.

The work was conducted as part of a larger effort directed toward developing the capability to treat a complete flight vehicle. Future work will be aimed at applications to more complex wing/fuselage geometries and developing a wing/fuselage/tail capability.

References

[1]Giesing, J. P., Kalman, T. P., and Rodden, W. P., "Subsonic Steady and Oscillatory Aerodynamics for Multiple Interfering Wings and Bodies," *Journal of Aircraft,* Vol. 9, Oct. 1972, pp. 693-702.

[2]Woodward, F. A., "Analysis and Design of Wing-Body Combinations at Subsonic and Supersonic Speeds," *Journal of Aircraft,* Vol. 5, Nov.-Dec. 1968, pp. 528-534.

[3]Woodward, F. A., "An Improved Method for the Aerodynamic Analysis of Wing-Body-Tail Configurations in Subsonic and Supersonic Flows," NASA CR-2228, May 1973.

[4]Dusto, A. R. and Epton, M. A., "An Advanced Panel Method for Analysis of Arbitrary Configurations in Unsteady Subsonic Flow," NASA CR-152323, Feb. 1980.

[5]Bailey, F. R. and Ballhaus, W. F., "Relaxation Methods for Transonic Flow About Wing-Cylinder Combinations and Lifting Swept Wings," *Lecture Notes in Physics,* Vol. 19, Springer-Verlag, New York, 1972, pp. 2-9.

[6]Klunker, E. B. and Newman, P. A., "Computation of Transonic Flow About Lifting Wing-Cylinder Combinations," *Journal of Aircraft,* Vol. 11, April 1974, pp. 254-256.

[7]Bailey, F. R. and Ballhaus, W. F., "Comparisons of Computed and Experimental Pressures for Transonic Flows About Isolated Wings and Wing-Fuselage Configurations," NASA SP-347, March 1975, pp. 1213-1231.

[8]Boppe, C. W., "Computational Transonic Flow About Realistic Aircraft Configurations," AIAA Paper 78-104, Jan. 1978.

[9]Boppe, C. W. and Stern, M. A., "Simulated Transonic Flows for Aircraft with Nacelles, Pylons, and Winglets," AIAA Paper 80-0130, Jan. 1980.

[10]Borland, C. J. and Rizzetta, D. P., "Nonlinear Transonic Flutter Analysis," *AIAA Journal,* Vol. 20, Nov. 1982, pp. 1606-1615.

[11]Batina, J. T., "Unsteady Transonic Flow Calculations for Interfering Lifting Surface Configurations," *Journal of Aircraft,* Vol. 23, May 1986, pp. 423-430.

[12]Borland, C. J., "Further Development of XTRAN3S Computer Program," NASA CR-172335, May 1984.

[13]Mason, W. H., Mackenzie, C., Stern, M., Ballhaus, W. F., and Frick, J., "An Automated Procedure for Computing the Three-Dimensional Transonic Flow Over Wing-Body Combinations, Including Viscous Effects," AFFDL-TR-77-122, Vol. I, Feb. 1978.

[14]Binion, T. W. Jr., "An Investigation of Three-Dimensional Wall Interference in a Variable Porosity Transonic Wind Tunnel," AEDC-TR-74-76, Oct. 1974.

[15]Treadgold, D. A., Jones, A. F., and Wilson, K. H., "Pressure Distribution Measured in the RAE 8 ft. × 6 ft. Transonic Wind Tunnel on RAE Wing 'A' in Combination with an Axi-Symmetric Body at Mach Numbers of 0.4, 0.8, and 0.9," *Experimental Data Base for Computer Program Assessment,* AGARD-AR-138, May 1979.

[16]Newman, P. A. and Allison, D. O., "Comparison of Interference-Free Numerical Results with Sample Experimental Data for the AEDC Wall-Interference Model at Transonic and Subsonic Flow Conditions," NASA TM X-71991, July 1974.

[17]Batina, J. T., "Unsteady Transonic Flow Calculations for Wing-Fuselage Configurations," AIAA Paper 86-0862, May 1986 (also NASA TM 87707, March 1986).